Elastic and inelastic scattering at low temperature in low-dimensional phononic structures

S. Withington* and D. J. Goldie
Cavendish Laboratory, JJ Thomson Avenue, Cambridge, United Kingdom
(Received 26 April 2012; revised manuscript received 8 November 2012; published 30 May 2013)

A technique is described for modeling the low-temperature thermal behavior of phononic components patterned into amorphous dielectric membranes, such as Si_xN_y. Ballistic, elastic diffusive, localized, and inelastic diffusive transport are included. The model is well suited to studying components where heat is carried by a discrete set of large-scale acoustic modes. The scheme gives not only the average fluxes of components having statistically characterized microstructure, but also the spread in behavior of notionally identical devices. It is applicable to a wide range of geometries. The method is illustrated by simulating the behavior of a number of simple structures and studying the interactions between the different transport mechanisms. A single-stage Fabry-Perot resonator is used to identify likely operating characteristics of phononic filters.

DOI: 10.1103/PhysRevB.87.205442 PACS number(s): 07.57.Kp, 95.55.Rg, 66.70.−f, 65.80.−g

I. INTRODUCTION

The emergence of precision techniques for patterning dielectric membranes has led to the possibility of manufacturing low-dimensional phononic structures that suppress low-temperature (<1 K) thermal conductance and thermal fluctuation noise. Components such as these would find widespread use in ultralow-noise detector and sensor technology, thermometry, and microrefrigeration.[1–3] For work to proceed, it is necessary to devise a model that can be used to design experiments, interpret data, and provide conceptual insights into the physical processes involved. It must be possible to include the properties of imperfect materials and to calculate the spread in behavior of notionally identical devices.

To date, most work has considered uniform microbridges whose widths $0.5 < b < 4$ μm and thicknesses $0.1 < t < 0.5$ μm are either comparable with or smaller than the characteristic phonon wavelengths, and whose lengths are either much larger, $l > 50$ μm,[4–9] or much smaller, $l < 0.5$ μm,[10] than the acoustic attenuation length. In the case of very short samples, the conductance is quantum limited and is determined solely by the number of propagating modes;[11,12] in the case of very long samples, the conductance falls as some function of l due to scattering.[13]

The scattering lengths of the microscopic processes responsible for absorption depend on the nature of the material. Acoustic attenuation in crystalline dielectrics is determined fundamentally by thermoelastic damping,[14] where the anharmonicity of the lattice couples the acoustic wave to a background of diffuse thermal excitations. At low temperatures in highly disordered dielectrics, such as low-stress Si_xN_y, the thermoelastic effect is swamped[15] by the excitation of two level systems (TLSs) associated with the reconfiguration of loosely bound atoms.[16–20] We have measured the specific heat of our own Si_xN_y on many occasions, and it is two orders of magnitude larger than the Debye value, which is a known feature of TLSs. In addition to these inelastic processes, surface roughness, defects, and voids lead to elastic scattering and to a reduction in thermal flux.

Linear chains of elastically coupled masses with damped Langevin terminations have been used to study the effects of disorder on heat transport in low-dimensional crystals.[21] Also, the nonequilibrium Greens function (NEGF) method has been used to look at the effect of isotopic disorder on heat flow in carbon and boron-nitride nanotubes.[22,23] In all cases, the transport changes from ballistic, to elastic diffusive, and to localized as the length of the sample is increased. Both of these approaches require physical models to be established at the atomic level and are not suitable for patterned mesoscopic structures where heat is carried by a small number of acoustic modes comprising the collective behavior of a large number of atoms. To model mesoscopic structures it is better to determine the dispersion relationships of the low-energy phonon modes by using an elastic continuum model, and then to include scattering through perturbation techniques. Procedures have been reported for incorporating imperfections such as surface roughness[4,24,25] and TLSs,[26] but they treat scattering as a surface-reflection phenomena and do not include localization, inelastic diffusive transport, or the effect of inelastic scattering on localization. Traditional Boltzmann transport formulations can be modified to include ballistic phonons,[27] but they do not accommodate resonant interactions and so do not account for localization and cannot be used for modeling patterned components such as Fabry-Perot resonators. These omissions are restrictive because thermal conductivity, heat capacity, and ultrasonic measurements on bulk samples show that glassy materials are strongly localized and exhibit high levels of acoustic loss.[28,29]

Against this background, we recently described a scheme[30] for modeling low-temperature heat flow in amorphous dielectric microbridges having acoustic loss. The loss absorbs and reradiates energy incoherently to yield an inelastic diffusive process. The model shows how the conductance changes smoothly from being ballistic to diffusive, with a $1/l$ dependence as the length of the sample is increased beyond the acoustic attenuation length. The approach emphasizes the difference between the physical scattering length and the acoustic attenuation length and points to the possible role of saturation.

In this paper, we show how elastic and inelastic scattering can be incorporated simultaneously into a multimode acoustic-wave model of patterned components. By combining a directed flow-graph technique to describe macroscopic elastic processes with a power balancing technique to describe inelastic absorption and reradiation, it is possible to accommodate

ballistic, inelastic-diffusive, elastic-diffusive, and localized transport. Moreover, it is suited to mesoscopic components, where the forms and dispersion relationships of the acoustic modes can be calculated easily. The use of directed flow graphs has a good heritage, because they are used extensively for short-wavelength electromagnetic calculations, often involving hundreds of traveling and evanescent waves and hundreds of scattering elements. They are used to describe waveguide components having complex profiles,[31] giving results that are in close agreement with high-dynamic-range measurements.

In our model, the dielectric structure being studied is divided into elements, each of which transmits, scatters, absorbs, and reradiates acoustic waves in the form of discrete modes. There are many techniques for calculating the forms and dispersion relationships of modes on mesoscopic dielectric bars having arbitrary cross sections,[32,33] including multilayers. The dynamical processes responsible for the losses are not modeled individually but are represented collectively through a local temperature that quantifies the occupancy of the extraneous degrees of freedom. In the case of amorphous dielectrics, TLSs interact through near-field effects, creating a heat reservoir to which the propagating phonon modes can couple. In principle, the model can be applied to any lossy system where there are local degrees of freedom that interact over short distances, including localized electron transport.

The elements of the structure may be uniform bars, steps in width, defects, etc. The behavior of each element is described by a scattering matrix that relates the incoming to the outgoing complex traveling-wave amplitudes. The losses may radiate acoustic waves, and so independent sources must be included for each element. The structure is terminated at each end by heat baths, which can also scatter and radiate acoustic energy. The linear relationship between all of the the sources and all of the traveling-wave amplitudes at every plane can be used to establish an equation that relates the correlations between the sources and traveling-wave amplitudes at every plane. At the outset, the temperature distribution along the structure is not known, but in the steady state the total power flow at every plane must be the same, and this condition can be used to find the temperature distribution that gives a self-consistent solution. Once the temperature distribution of the losses is known, many other aspects of behavior can be calculated.

A desirable feature of the scheme is that the material is characterized by elastic constants, including loss, which can be regarded as parameters when modeling and fitting experimental data, regardless of the specific mechanisms responsible for the loss. The origin of losses varies widely between materials and is highly dependent on the deposition and patterning processes used.

II. MICROBRIDGE THEORY

The transmission and scattering of waves on a dielectric bar can be represented as a linear process by the directed graph shown in Fig. 1. More complicated multiport arrangements, representing more complicated thermal structures, are possible. The complex acoustic-wave spectral amplitudes $\mathbf{a}_n$ and $\mathbf{b}_n$ traveling to the right and left respectively at reference plane n

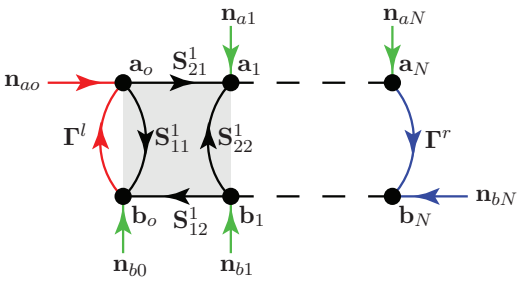

FIG. 1. (Color online) Directed flow graph of a microbridge. The hot load $\mathbf{n}_{a0}$ is on the left (red), and the cold load $\mathbf{n}_{bN}$ is on the right (blue). $\mathbf{n}_{a1}$ to $\mathbf{n}_{aN}$, and $\mathbf{n}_{b0}$ to $\mathbf{n}_{b(N-1)}$, are the noise waves (green) injected by losses. The shaded area shows element 1 having scattering matrices $\mathbf{S}^1_{ij}$ and noise sources $\mathbf{n}_{b0}$ and $\mathbf{n}_{a1}$.

can be assembled into a column vector $\mathbf{v}$:

$$\mathbf{v} = [\mathbf{a}_0, \mathbf{a}_1, \mathbf{a}_2, \mathbf{a}_n, \mathbf{a}_N;\ \mathbf{b}_0, \mathbf{b}_1, \mathbf{b}_2, \mathbf{b}_n, \mathbf{b}_N]^T . \tag{1}$$

$\mathbf{a}_n$ and $\mathbf{b}_n$ are themselves vectors because a number of forward- and backward-traveling modes are present at each plane in the structure. T denotes the transpose. It is straightforward to include evanescent waves, but we shall not do so here. Each element represents some physical feature of the component: uniform bar, step discontinuity, void, junction, etc. The mode amplitudes are analytic signals and are normalized so that the square amplitude is the power traveling in the given direction at the associated plane. It is not necessary to use the same number of modes for each element, but if the same number is used, say M, then $\mathbf{v} \in \mathbb{C}^{2(N+1)M}$.

For each element there is a block scattering matrix $\mathbf{S}$ that describes the linear relationship between the incoming and outgoing waves. For the nth element,

$$\begin{bmatrix} \mathbf{b}_{n-1} \\ \mathbf{a}_n \end{bmatrix} = \underbrace{\begin{bmatrix} \mathbf{S}^n_{11} & \mathbf{S}^n_{12} \\ \mathbf{S}^n_{21} & \mathbf{S}^n_{22} \end{bmatrix}}_{\mathbf{S}^n} \begin{bmatrix} \mathbf{a}_{n-1} \\ \mathbf{b}_n \end{bmatrix}, \tag{2}$$

where subscripts distinguish the blocks. $\mathbf{S}^n_{11}$ and $\mathbf{S}^n_{22}$ represent the reflections from the input and output ports of element n, respectively, and $\mathbf{S}^n_{21}$ and $\mathbf{S}^n_{12}$ represent the forward- and backward-scattering processes. There are many techniques based on elasticity theory for calculating these matrices. The ends of the microbridge are terminated by one-port components, which constitute the heat baths. $\mathbf{a}_0 = \mathbf{\Gamma}^l \mathbf{b}_0$, where $\mathbf{\Gamma}^l$ is the scattering matrix of the left termination, and $\mathbf{b}_N = \mathbf{\Gamma}^r \mathbf{a}_N$, where $\mathbf{\Gamma}^r$ is the scattering matrix of the right termination. In the perfectly absorptive case, $\mathbf{\Gamma}^l = \mathbf{\Gamma}^r = \mathbf{0}$.

To develop the model it is necessary to include the acoustic noise waves radiated by the terminations and by the losses in the elements themselves. The waves radiated by an element are temporally phase incoherent with respect to the incoming and elastically scattered waves and can be represented on the directed graph as independent sources. The complex amplitudes of these sources can be assembled into a vector $\mathbf{n}$,

$$\mathbf{n} = [\mathbf{n}_{a0}, \mathbf{n}_{a1}, \mathbf{n}_{a2}, \mathbf{n}_{an}, \mathbf{n}_{aN};\ \mathbf{n}_{b0}, \mathbf{n}_{b1}, \mathbf{n}_{b2}, \mathbf{n}_{bn}, \mathbf{n}_{bN}]^T , \tag{3}$$

where $\mathbf{n}_{a1}$ should be interpreted as the acoustic noise waves that effectively combine with $\mathbf{a}_1$ at node 1, etc.

It is convenient to distinguish explicitly between internal noise waves $\mathbf{n}^i$, which originate from acoustic losses, and external noise waves $\mathbf{n}^e$, which are injected by the warm terminations: $\mathbf{n} = \mathbf{n}^i + \mathbf{n}^e$. For the microbridge shown in Fig. 1,

$$\begin{aligned}\mathbf{n}^i &= [\mathbf{0},\mathbf{n}_{a1},\mathbf{n}_{a2},\mathbf{n}_{an},\mathbf{n}_{aN};\ \mathbf{n}_{b0},\mathbf{n}_{b1},\mathbf{n}_{b2},\mathbf{n}_{bn},\mathbf{0}]^T,\\ \mathbf{n}^e &= [\mathbf{n}_{a0},\mathbf{0},\mathbf{0},\mathbf{0},\ldots,\mathbf{0};\ \mathbf{0},\mathbf{0},\mathbf{0},\mathbf{0},\ldots,\mathbf{n}_{bN}]^T.\end{aligned} \tag{4}$$

Given a set of internal and external sources, $\mathbf{n}^i$ and $\mathbf{n}^e$, it is possible to calculate the complex amplitudes of the traveling-wave amplitudes at every plane. One might imagine that it is best to solve the problem by using a cascade of transmission matrices as is done in multimode electromagnetic calculations,[31] but this approach is not suitable here. The difference is that in electromagnetic calculations all of the sources are at one end of the system and it is only necessary to calculate the dependent variables at the other; in thermal calculations, sources are present along the whole length of the structure, and it is necessary to calculate the dependent variables everywhere. The latter problem can be solved by establishing a block matrix $\mathbf{P}$ that contains information about all of the interconnections in the system. Each entry is the complex transmission matrix connecting the respective nodes.

When no sources are present, the dependencies are described by $\mathbf{v} = \mathbf{P}\mathbf{v}$, but when sources are included

$$\mathbf{v} = \mathbf{P}\mathbf{v} + \mathbf{n}^i + \mathbf{n}^e, \tag{5}$$

which can be written

$$[\mathbf{I} - \mathbf{P}]\,\mathbf{v} = \mathbf{n}^i + \mathbf{n}^e, \tag{6}$$

where $\mathbf{I}$ is the identity matrix. Equation (6) can be inverted through $\mathbf{Q} = [\mathbf{I} - \mathbf{P}]^{-1}$, where the pseudo-inverse may be used, and then

$$\mathbf{v} = \mathbf{Q}[\mathbf{n}^i + \mathbf{n}^e], \tag{7}$$

which allows the traveling-wave amplitudes $\mathbf{v}$ to be calculated if all of the sources $\mathbf{n}^i$ and $\mathbf{n}^e$ are known.

For a single-mode microbridge, $\mathbf{P}$ can be written down easily through inspection of Fig. 1, and $\mathbf{I} - \mathbf{P}$ becomes

$$\mathbf{I} - \mathbf{P} = \left[\begin{array}{ccccc|ccccc} 1 & 0 & 0 & 0 & 0 & -\Gamma_1 & 0 & 0 & 0 & \\ -S_{21}^1 & 1 & 0 & 0 & 0 & 0 & -S_{22}^1 & 0 & 0 & 0 \\ 0 & -S_{21}^2 & 1 & 0 & 0 & 0 & 0 & -S_{22}^2 & 0 & 0 \\ 0 & 0 & -S_{21}^n & 1 & 0 & 0 & 0 & 0 & -S_{22}^n & 0 \\ 0 & 0 & 0 & -S_{21}^N & 1 & 0 & 0 & 0 & 0 & -S_{22}^N \\ \hline -S_{11}^1 & 0 & 0 & 0 & 0 & 1 & -S_{12}^1 & 0 & 0 & 0 \\ 0 & -S_{11}^2 & 0 & 0 & 0 & 0 & 1 & -S_{12}^2 & 0 & 0 \\ 0 & 0 & -S_{11}^n & 0 & 0 & 0 & 0 & 1 & -S_{12}^n & 0 \\ 0 & 0 & 0 & -S_{11}^N & 0 & 0 & 0 & 0 & 1 & -S_{12}^N \\ 0 & 0 & 0 & 0 & -\Gamma_2 & 0 & 0 & 0 & 0 & 1 \end{array}\right]. \tag{8}$$

In this case, $\mathbf{P}$ is sparse because only a small fraction of all possible connections are present. Nevertheless, for flexibility, because of the ease of setting up the connection matrix of any general system, and because sparse-matrix inversion techniques are readily available, we adopt this approach.

A complicating factor is that we must describe the process in terms of the correlations between the traveling-wave amplitudes because the complex values of the sources are not known. To handle partial coherence, form the correlation matrix of the nodal variables, $\mathbf{V} = \langle \mathbf{v}\mathbf{v}^\dagger \rangle$, then according to Eq. (7)

$$\begin{aligned}\mathbf{V} &= \mathbf{Q}\langle[\mathbf{n}^i + \mathbf{n}^e][\mathbf{n}^i + \mathbf{n}^e]^\dagger\rangle\mathbf{Q}^\dagger\\ &= \mathbf{Q}\mathbf{N}^i\mathbf{Q}^\dagger + \mathbf{Q}\mathbf{N}^e\mathbf{Q}^\dagger,\end{aligned} \tag{9}$$

where the second line follows because the external and internal sources are uncorrelated. $\mathbf{V}$ can be expressed as a block matrix to distinguish the correlations:

$$\mathbf{V} \equiv \begin{bmatrix} \mathbf{A} & \mathbf{C} \\ \mathbf{C}^\dagger & \mathbf{B} \end{bmatrix}. \tag{10}$$

$\mathbf{A}$, $\mathbf{B}$, and $\mathbf{C}$ carry information about the correlations between the forward-traveling waves, backward-traveling waves, and forward- and backward-traveling waves, respectively. These matrices can also be expressed in terms of blocks: $\mathbf{A}_{11} = \langle \mathbf{a}_1\mathbf{a}_1^\dagger \rangle$, $\mathbf{B}_{11} = \langle \mathbf{b}_1\mathbf{b}_1^\dagger \rangle$, etc., which give the correlations between the complex wave amplitudes at different planes.

For constant-temperature thermal sources, the correlations are statistically stationary, different frequency components are uncorrelated, and the net fluxes are found by integrating with respect to frequency. The expectation value of the net backward-traveling power at plane i is

$$P_i = \int \mathrm{Tr}\,[\mathbf{B}_{ii}(\nu) - \mathbf{A}_{ii}(\nu)]\,d\nu, \tag{11}$$

where spectral dependence is shown explicitly. It follows that for any external noise-source correlation matrix $\mathbf{N}^e(\nu)$ and any assumed internal noise-source correlation matrix $\mathbf{N}^i(\nu)$, it is possible, through Eqs. (9)–(11), to determine the power flow at each plane. In the steady state, however, the power flow at every plane must be the same, $P = P_i\ \forall\ i \in \{0,\ldots,N\}$,

where P is the net equilibrium power flow at every point on the structure.

Two questions remain: (i) How can the noise-source correlation matrices $\mathbf{N}^i$ be found once the scattering matrices are known? (ii) How can the temperatures of the internal degrees of freedom that constitute the losses be found?

Consider (i). From Eqs. (2) and (3), for element n,

$$\begin{aligned}\begin{bmatrix} \langle \mathbf{b}_{n-1}\mathbf{b}_{n-1}^{\dagger}\rangle & \langle \mathbf{b}_{n-1}\mathbf{a}_{n}^{\dagger}\rangle \\ \langle \mathbf{a}_{n}\mathbf{b}_{n-1}^{\dagger}\rangle & \langle \mathbf{a}_{n}\mathbf{a}_{n}^{\dagger}\rangle \end{bmatrix} &= \mathbf{S}^{n}\begin{bmatrix} \langle \mathbf{a}_{n-1}\mathbf{a}_{n-1}^{\dagger}\rangle & \langle \mathbf{a}_{n-1}\mathbf{b}_{n}^{\dagger}\rangle \\ \langle \mathbf{b}_{n}\mathbf{a}_{n-1}^{\dagger}\rangle & \langle \mathbf{b}_{n}\mathbf{b}_{n}^{\dagger}\rangle \end{bmatrix}\mathbf{S}^{n\dagger} \\ &+ \begin{bmatrix} \langle \mathbf{n}_{b(n-1)}\mathbf{n}_{b(n-1)}^{\dagger}\rangle & \langle \mathbf{n}_{b(n-1)}\mathbf{n}_{an}^{\dagger}\rangle \\ \langle \mathbf{n}_{an}\mathbf{n}_{b(n-1)}^{\dagger}\rangle & \langle \mathbf{n}_{an}\mathbf{n}_{an}^{\dagger}\rangle \end{bmatrix}, \end{aligned} \tag{12}$$

where the internal sources associated with the losses have been included. Equation (12) can be written

$$\begin{aligned}\begin{bmatrix} \mathbf{B}_{n-1,n-1} & \mathbf{C}_{n,n-1}^{\dagger} \\ \mathbf{C}_{n,n-1} & \mathbf{A}_{n,n} \end{bmatrix} &= \mathbf{S}^{n}\begin{bmatrix} \mathbf{A}_{n-1,n-1} & \mathbf{C}_{n-1,n} \\ \mathbf{C}_{n-1,n}^{\dagger} & \mathbf{B}_{n,n} \end{bmatrix}\mathbf{S}^{n\dagger} \\ &+ \begin{bmatrix} \mathbf{Nb}_{n-1,n-1} & \mathbf{Nc}_{n,n-1}^{\dagger} \\ \mathbf{Nc}_{n,n-1} & \mathbf{Na}_{n,n} \end{bmatrix}. \end{aligned} \tag{13}$$

Now imagine that element n is isolated and illuminated on both sides by incoming uncorrelated waves from perfectly matched thermal sources having the same temperature T_n as the element itself,

$$\begin{bmatrix} \mathbf{A}_{n-1,n-1} & \mathbf{C}_{n-1,n} \\ \mathbf{C}_{n-1,n}^{\dagger} & \mathbf{B}_{n,n} \end{bmatrix} = U(T_n,\nu)\begin{bmatrix} \mathbf{I} & \mathbf{0} \\ \mathbf{0} & \mathbf{I} \end{bmatrix}, \tag{14}$$

where $U(T_n,\nu)$ is the Planck distribution:

$$U(T_n,\nu) = \frac{h\nu}{e^{h\nu/kT_n}-1}. \tag{15}$$

Because the element and sources are at the same physical temperature, it is not possible to distinguish between the radiation produced by the external sources and the radiation produced by the internal sources. The outgoing waves must be uncorrelated and have the same radiative temperature:

$$\begin{bmatrix} \mathbf{B}_{n-1,n-1} & \mathbf{C}_{n,n-1}^{\dagger} \\ \mathbf{C}_{n,n-1} & \mathbf{A}_{n,n} \end{bmatrix} = U(T_n,\nu)\begin{bmatrix} \mathbf{I} & \mathbf{0} \\ \mathbf{0} & \mathbf{I} \end{bmatrix}. \tag{16}$$

Equations (13) to (16) then give

$$\begin{bmatrix} \mathbf{Nb}_{n-1,n-1} & \mathbf{Nc}_{n,n-1)}^{\dagger} \\ \mathbf{Nc}_{n,n-1)} & \mathbf{Na}_{n,n} \end{bmatrix} = [\mathbf{I}-\mathbf{S}^{n}\mathbf{S}^{n\dagger}]U(T_n,\nu). \tag{17}$$

In electromagnetic-systems analysis, this approach is known as Bosma's theory,[34,35] and it is equally applicable here. Thus, once the scattering parameters are known, and the temperature of the element is known, the internal source correlation matrix can be found. The only restriction is that the overall structure must be sampled finely enough to ensure that the temperature distribution is represented accurately.

The same reasoning allows the external noise-source correlation matrices of the heat baths to be found:

$$\mathbf{Na}_{0,0} = [\mathbf{I}-\mathbf{\Gamma}^{l}\mathbf{\Gamma}^{l\dagger}]U(T_h,\nu), \tag{18}$$

and

$$\mathbf{Nb}_{N,N} = [\mathbf{I}-\mathbf{\Gamma}^{r}\mathbf{\Gamma}^{r\dagger}]U(T_c,\nu), \tag{19}$$

where T_h and T_c are the temperatures of the hot and cold terminations, respectively. Thus, if the temperatures of the terminations and elements are known, Eqs. (9), (17), (18), and (19) can be used to calculate the net heat flow at every plane. In fact, it is possible to calculate the correlations between any pair of the traveling-wave amplitudes.

Turning to (ii). The temperatures of the elements are not known in advance and must be found. In the case of a single-mode microbridge there are $N+1$ unknowns: the temperatures T_1 to T_N, and the net heat flow P. Likewise, there are $N+1$ equations: the net heat flow at each of the planes, which are not equal if the temperature distribution differs from that of the steady state. To find a solution, make a first guess at the element temperatures, assemble them into a vector $\mathbf{t}$, and calculate the vector-valued function $\mathbf{s}(\mathbf{t})$ that gives the frequency-integrated power flow at every plane: $\mathbf{t}\in\mathbb{R}^N$, $\mathbf{s}(\mathbf{t})\in\mathbb{R}^{N+1}$. At equilibrium $P\mathbf{s}_0=\mathbf{s}(\mathbf{t})$, where $\mathbf{s}_0$ is a column vector of ones, because the power flow at every plane must be the same. Generally, the first guess is wrong, the net flux into each cell is not zero, and an error vector results:

$$\mathbf{\Delta}(\mathbf{x}) = P\mathbf{s}_0 - \mathbf{s}(\mathbf{t}). \tag{20}$$

The error $\mathbf{\Delta}(\mathbf{x})$ is a function of the unknown state vector $\mathbf{x}$, which comprises P and $\mathbf{t}$. $\mathbf{\Delta}(\mathbf{x})$ has dimension $N+1$, where each entry is a nonlinear function of the $(N+1)$-dimensional state vector $\mathbf{x}$. This function has the same number of equations as unknowns and in principle can be solved uniquely, although its conditioning is not known.

It is necessary to solve $\mathbf{\Delta}(\mathbf{x})=\mathbf{0}$, which can be achieved through the iterative Newton procedure

$$\mathbf{x}^{k+1} = \mathbf{x}^{k} - \chi[\mathbf{J}(\mathbf{x}^{k})]^{-1}\mathbf{\Delta}(\mathbf{x}^{k}), \tag{21}$$

where χ is a convergence parameter between zero and unity, typically 0.8. Its actual value does not change the result, only the speed and stability of convergence. The elements of the Jacobian $\mathbf{J}(\mathbf{x})$ are the rates of change of the elements of the error vector $\mathbf{\Delta}(\mathbf{x})$ with respect to the elements of the state vector $\mathbf{x}$. The sequence (21) has a quadratic rate of convergence near the solution and is highly efficient.

The only remaining question is what temperature distribution $\mathbf{t}$, and what flux P, should be used as the starting guess? Often, it is sufficient to assume that all quantities are zero, or that the temperatures are distributed linearly between the two end temperatures. When performing a series of simulations, say when sweeping one of the termination temperatures, it is beneficial to use the solution of the previous calculation as the starting guess of the next.

We have been cavalier when comparing the number of equations with the number of unknowns. Consider a structure comprising a number of uniform bars having different widths separated by discontinuous steps. Each of the bars and steps is represented by a scattering matrix, but whereas the bars generally exhibit loss, the steps do not. Therefore, it does not make sense to allocate temperatures to those elements that are lossless. In fact, Eq. (17) returns a zero result for the noise-source correlation matrix. In the case of lossless

elements, the *net* flux traveling across the input plane is equal to the *net* flux traveling across the output plane, and only one of the two planes needs to be included in the iterative analysis, reducing the number of available equations by one. Likewise, the temperature of the cell does not enter, reducing the number of unknowns by one. The number of unknowns is still equal to the number of equations regardless of the number of lossless elements. Generally, any connected lossless elements can be lumped together and not allocated a temperature. If the whole system is lossless, an iterative calculation is not needed at all. When the iterative routine is needed, we have found that it converges reliably over a wide variety of structures, taking only 5–10 iterations to achieve errors of less than 0.1% on all variables.

III. SCATTERING MATRICES

The model can incorporate any number of modes having different characteristics and, by using modal scattering calculations based on continuum mechanics, can take into account mode conversion at steps, along profiled structures, and at defects.[36–38] At very low temperatures, only acoustic phonon modes are important, and just four modes continue to propagate as $\nu \to 0$: longitudinal, torsional, in-plane flexure, and out-of-plane flexure. For illustration we shall consider the modes and reflections at a step change in width of a rectangular bar.[39] A change in thickness is straightforward to accommodate.

Longitudinal. The longitudinal mode has a linear dispersion relationship $\omega = c_l k$ where $c_l = \sqrt{E/\rho}$ is the longitudinal sound speed, E is Young's modulus, and ρ is the density. The wave impedance is $Z_l = \sqrt{E\rho}A$, where $A = bt$ is the cross-sectional area, b is the width, and t is the thickness. A discontinuity in impedance can occur because of changes in the density, elastic constants, or cross section. If we attribute every discontinuity to a change in width, the scattering matrix becomes

$$\mathbf{S}_l = \begin{bmatrix} (1-h)/(1+h) & 2\sqrt{h}/(1+h) \\ 2\sqrt{h}/(1+h) & (h-1)/(h+1) \end{bmatrix}, \tag{22}$$

where $h = b_2/b_1$, and b_1 and b_2 are the widths of the bars on the input and output sides, respectively. Equation (22) has been normalized so that the square-magnitudes of the mode coefficients give the power flow on each side of the step. If h is large or small the reflection coefficients tend to ± 1, which occurs because large-area bars are stiff.

Torsional. The lowest-order torsional mode has the dispersion relationship $\omega = 2c_t(t/b)k$, where $c_t = \sqrt{\mu/\rho}$ is the transverse sound speed and μ is the shear modulus. The torsional mode has the impedance $Z_t = \sqrt{\mu\rho}A^2/6$, where it is assumed that one dimension is much smaller than the other, $t < b$. The scattering matrix for the normalized mode coefficients is

$$\mathbf{S}_t = \begin{bmatrix} (1-h^2)/(1+h^2) & 2h/(1+h^2) \\ 2h/(1+h^2) & (h^2-1)/(h^2+1) \end{bmatrix}. \tag{23}$$

Flexural. The two flexural modes, which are degenerate for a square bar, have quadratic dispersion relationships. For out-of-plane flexure, $\omega = c_l\sqrt{t^2/12}k^2$, whereas for in-plane flexure $\omega = c_l\sqrt{b^2/12}k^2$. For out-of-plane flexure, the complex reflection r and transmission t parameters are found through

$$\begin{bmatrix} r \\ t \\ d_- \\ d_+ \end{bmatrix} = \begin{bmatrix} 1 & -1 & 1 & -1 \\ 1 & 1 & i & i \\ 1 & -h & -1 & h \\ 1 & h & -i & -ih \end{bmatrix}^{-1} \begin{bmatrix} -1 \\ 1 \\ -1 \\ 1 \end{bmatrix}, \tag{24}$$

where d_- and d_+ are the amplitudes of the evanescent waves on either side of the junction, which are needed to satisfy the boundary conditions[39] but which are not taken into account further. In order to calculate the normalized scattering matrix, we must multiply the forward-transmission parameter t_{21} by $\sqrt{Z_2/Z_1}$ and the reverse transmission parameter t_{12} by $\sqrt{Z_1/Z_2}$, where Z_1 and Z_2 are the characteristic impedances on each side of the step. The impedance of the out-of-plane flexural mode is given by $Z_{of} = \sqrt{E\rho}(A/\sqrt{12})tk$, which depends on frequency through k, but in this case $k_1 = k_2$ because $t_1 = t_2$, and therefore

$$\mathbf{S}_{of} = \begin{bmatrix} r_{11} & t_{12}h^{-1/2} \\ t_{21}h^{1/2} & r_{22} \end{bmatrix}. \tag{25}$$

The quantities r_{11} and r_{22} have the same sign for large changes in width and are both purely imaginary as a consequence of the energy stored in the evanescent fields.

For in-plane flexure, the complex reflection and transmission parameters are found through

$$\begin{bmatrix} r \\ t \\ d_- \\ d_+ \end{bmatrix} = \begin{bmatrix} 1 & -1 & 1 & -1 \\ 1 & h^{-1/2} & i & ih^{-1/2} \\ 1 & -h^2 & -1 & h^2 \\ 1 & h^{3/2} & -i & -ih^{3/2} \end{bmatrix}^{-1} \begin{bmatrix} -1 \\ 1 \\ -1 \\ 1 \end{bmatrix}. \tag{26}$$

The impedance of the in-plane flexural mode is given by $Z_{if} = \sqrt{E\rho}(A/\sqrt{12})bk$, which depends on frequency through k, but now $k_1 \neq k_2$ because $b_1 \neq b_2$, and therefore

$$\mathbf{S}_{if} = \begin{bmatrix} r_{11} & t_{12}h^{-3/4} \\ t_{21}h^{3/4} & r_{22} \end{bmatrix}. \tag{27}$$

Again, r_{11} and r_{22} are both purely imaginary for large changes in width.

All of the characteristic impedances are real, none of the scattering matrices depend on frequency, and all of the scattering matrices are lossless and therefore unitary. Figure 2

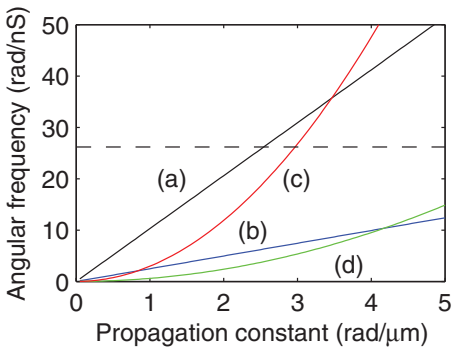

FIG. 2. (Color online) Dispersion relationships of the (a) longitudinal, (b) torsional, (c) in-plane flexural, and (d) out-of-plane flexural modes of Si_xN_y. The bar is 0.2 μm thick and 1 μm wide. The dashed line corresponds to $2kT/\hbar$ at $T = 0.1$ K.

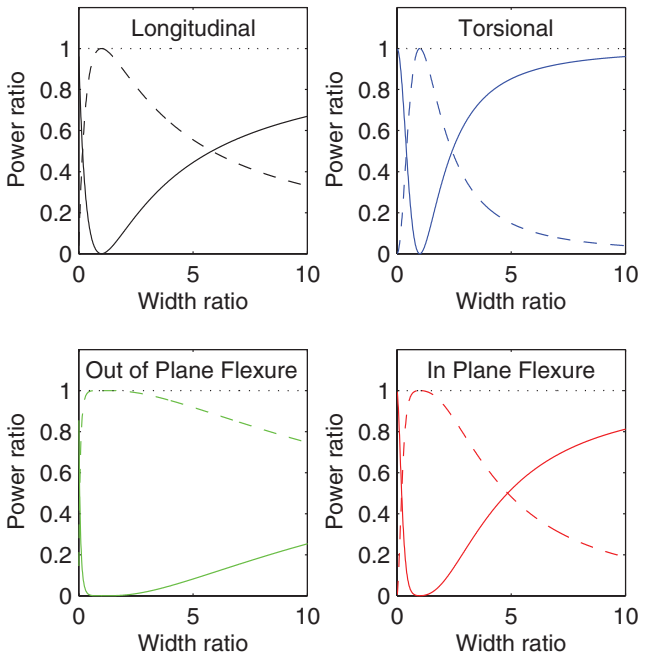

FIG. 3. (Color online) Power transmission (dashed) and reflection (solid) of different modes as a function of the ratio of output width to input width of a step discontinuity. The dotted lines show the sum of the two, indicating that steps are lossless. The colors correspond to those of Fig. 2.

shows the dispersion relationships of the (a) longitudinal, (b) torsional, (c) in-plane flexural, and (d) out-of-plane flexural modes of a Si_xN_y microbridge, 0.2 μm thick and 1 μm wide. We have used $c_l \approx 10\,300$ km/s and $c_t \approx 6200$ km/s. The dotted line shows $2kT/\hbar$ at 0.1 K, which indicates a typical level of excitation. Note that the torsional and out-of-plane flexural modes have low phase and group velocities compared with the longitudinal and in-plane flexural modes, indicating their relative compliance. Figure 3 shows the power transmission (dashed) and reflection (solid) coefficients of a step discontinuity as a function of the ratio h of the output width to the input width. The four plots correspond to the longitudinal (black), torsional (red), out-of-plane flexural (green), and in-plane flexural (red) modes. The dotted lines show the sum of the reflected and transmitted power, confirming that the discontinuity is lossless. The plots have certain features in common as a consequence of the reflection coefficient tending to unity for extreme steps, the need for the reflection to be zero when there is no step, and for the plots to be unchanged when the step is viewed from the other side $h \to 1/h$. There are, however, differences: the out-of-plane flexural mode is only reflected weakly for steps of modest size, whereas the torsional mode is very sensitive to steps. Although it would be straightforward to take into account mode conversion at steps, we shall not do so here.

To complete the scheme, we require the scattering matrices of uniform bars. For a single mode,

$$\mathbf{S}_b = \begin{bmatrix} 0 & G(\nu)\exp[ik\Delta l] \\ G(\nu)\exp[ik\Delta l] & 0 \end{bmatrix}, \qquad (28)$$

where Δl is the length of the section, and a frequency-dependent transmission factor $G(\nu)$ has been included to represent the acoustic loss. Only frequency dependence has been shown explicitly, but other dependencies can be included. For multimode systems, more terms can be added, but the principle remains the same.

IV. SIMULATIONS

Consider a uniform, single-mode microbridge. To eventually allow for step discontinuities, 100 bars and 200 scattering matrices were used. The transmission per bar was $G = 0.9$, which corresponds to having inelastic, but no elastic, scattering. The matched terminations were held at $T_h = 0.3$ K and $T_c = 0.1$ K, and $\nu = 5$ GHz. The routine adjusted 100 temperatures to calculate the correlations between 400 traveling-wave amplitudes. Figure 4 shows the expectation values of the forward and backward fluxes, and the temperatures of the internal degrees of freedom that constitute the losses, as a function of position. The top and bottom solid (black) lines show the powers flowing to the right and left, respectively. The difference between the two, indicated by the dotted line, is the net power, which must be everywhere the same in the steady state. Each of the solid (black) lines comprises two parts: a decaying ballistic part (red), and a growing radiated part (green). The ballistic and radiated fluxes combine to form the total forward and backward fluxes, which are linear functions of position. Because the ballistic and radiated waves are phase incoherent, it is appropriate to add the fluxes in this way. The diffusive nature of the process is clear because the ballistic parts are attenuated severely, but there is a flow of

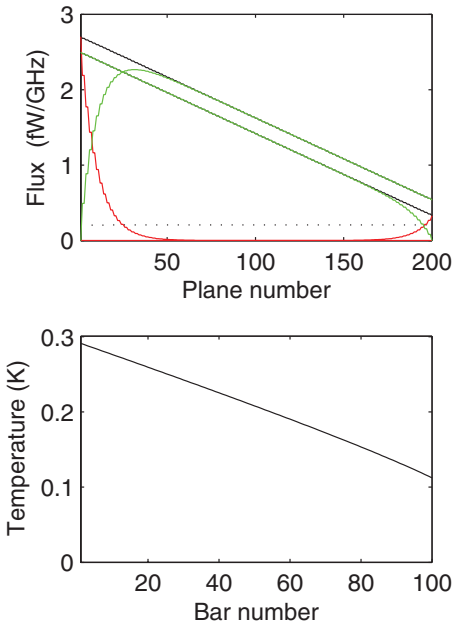

FIG. 4. (Color online) Simulation of a uniform, single-mode microbridge. The structure has inelastic, $G = 0.9$, but no elastic, scattering. $T_h = 0.3$ K, $T_c = 0.1$ K, and $\nu = 5$ GHz. Top: The top and bottom black lines show the power flowing to the right and left respectively. The dotted line shows the net power flowing along the structure. The red and green lines indicate the ballistic and diffusive contributions. Bottom: The temperature distribution of the losses.

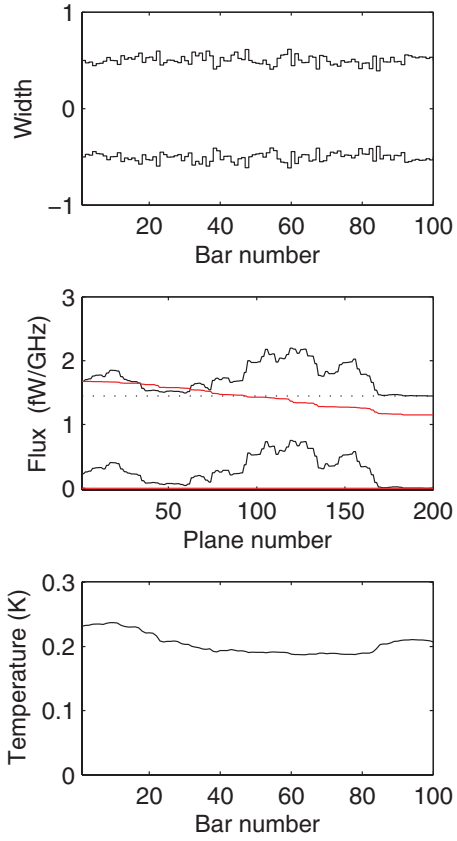

FIG. 5. (Color online) Top: Width, in normalized units, as a function of position. The structure had elastic but no inelastic $G = 0.999\,999$ scattering. $T_h = 0.3$ K, $T_c = 0.1$ K, and $\nu = 10$ GHz. Middle: The top and bottom black lines show the power flowing to the right and left, respectively. The dotted line shows the net power. The remaining (red) lines show the ballistic parts of the forward- and backward-traveling waves. Bottom: The temperature distribution of the poorly coupled losses.

power due to heating and reradiation. The ballistic-diffusive theory of heat conduction makes a similar distinction, but with the transport described in terms of the carrier distribution function.[27] The bottom plot in Fig. 4 shows the temperature of the losses as a function of position. The distribution is slightly curved, because the internal source flux has to be a linear function of position, but the source flux is not linearly related to temperature.[30] Certain features, such as the discontinuities at the ends, have been observed previously in the context of solutions of the Boltzmann transport equation.[27,40–42]

Figure 5 shows the behavior of a nonuniform, essentially lossless microbridge, $G = 0.999\,999$. The matched terminations were held at $T_h = 0.3$ K and $T_c = 0.1$ K. To demonstrate the effects of elastic scattering, the cross section was varied by drawing widths from a random Gaussian population having $b = 1.0 \pm 0.1$. Because the widths enter only through ratios h, units are not specified. The number of bars used was 100, each having a length of $\Delta l/\lambda = 0.02$ at 1 GHz. In the case of Si_xN_y, the parameters correspond to a 20-μm-long sample having a surface-roughness correlation length of 0.2 μm. In practice, the discontinuities might be due to edge and surface roughness, changes in material properties, internal defects, etc., but for presentation purposes we attribute them to edge roughness and show the cross section as a symmetrical change in width. Other statistical models could be used. $\nu = 10$ GHz, which equates to having five bars per wavelength, with a roughness correlation length of 0.2 wavelengths. The top and bottom solid (black) lines of the middle plot show the powers traveling to the right and left, respectively. They combine to form the net flux, shown as a dotted line. The remaining (red) lines show the ballistic parts of the two oppositely directed fluxes. Only the ballistic flux traveling to the right is nonzero because $T_c = 0$ K. The ballistic fluxes were calculated by setting the reflective elements S_{11} and S_{22} of all of the cell scattering parameters to zero. It does not make sense to show scattered fluxes, because the scattered waves are phase coherent with respect to the incident waves, and so the fluxes do not add. This aspect of our model is different from the ballistic-diffusion equations.[27] The forward-traveling ballistic flux falls as a function of position due to scattering by individual discontinuities.

There are regions where the forward flux is higher than the flux injected at the hot end, and the backward flux is nonzero despite the cold termination being at 0 K. The resonant trapping of energy, or equivalently the localization of phonons, has appeared in a natural way.[43–45] When the model is run many times, using different profiles taken from the same statistical distribution, the behavior varies markedly. It is not usually possible to identify specific features in the profile that are responsible for the trapping seen. The bottom plot in Fig. 5 shows the temperature of the losses as a function of position. An identical simulation, but of a uniform microbridge, gives a temperature distribution that is constant at 0.22 K. This situation occurs because the internal losses are only lightly coupled to the two counter-propagating acoustic waves and so drift up to an intermediate temperature.[30] A similar effect is seen in Fig. 5, but with additional structure due to localization.

Matrix $\mathbf{V}$ in Eq. (10) contains the correlations between the traveling-wave amplitudes at different planes. Figure 6 shows the magnitudes of the correlation coefficients between the forward-traveling waves when plane 150 was used as the reference. The bottom (red) line corresponds to Fig. 4. In this case, phase-incoherent reradiation leads to decorrelation on the scale size of the acoustic attenuation length. The top (green) line corresponds to Fig. 5. In this case, the waves in both directions and at all planes are fully correlated, even

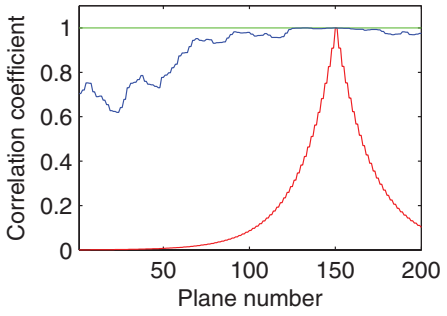

FIG. 6. (Color online) Magnitude of the correlation coefficients between the forward traveling waves at different positions, referenced to plane 150. The bottom (red) line corresponds to the inelastic case of Fig. 4, the top (green) line to the elastic case of Fig. 5, and the middle (blue) line to an elastic case having $T_h = T_c = 0.3$ K.

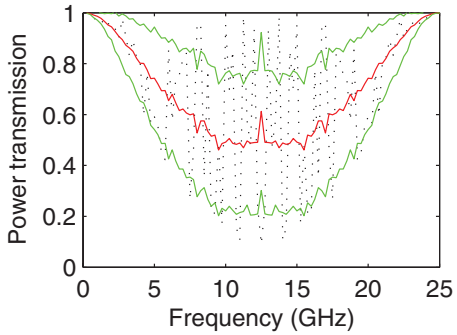

FIG. 7. (Color online) Transmission as a function of frequency for a single-mode microbridge having elastic scattering only. $T_h = 0.3$ K and $T_c = 0.0$ K. The profile was chosen randomly from a Gaussian distribution having $b = 1.0 \pm 0.1$. The dotted line shows the transmission of a single sample. The central (red) line show the average of 200 similar calculations having different profiles. The top and bottom (green) lines show the one-standard-deviation limits.

though a complex sequence of scattering events is taking place. The middle (blue) line corresponds to a fully elastic calculation, similar to that of Fig. 5, but with $T_h = T_c = 0.3$ K. Decorrelation occurs because, upon moving along the structure, the relative contributions from the uncorrelated hot and cold terminations change. On the left, the probability that the flux traveling to the right originates from the source on the left is higher than the probability of it originating from the source on the right; on the right, the opposite is true.

Figure 7 shows the normalized transmission of a single-mode microbridge as a function of frequency. The dotted line shows the behavior of a single sample having $T_h = 0.3$ K and $T_c = 0$ K. Only elastic scattering was included, with the position-dependent width drawn from a Gaussian population having $b = 1.0 \pm 0.1$. In this case, it was not necessary to perform an iterative calculation, and the fluxes were found directly by solving Eq. (9) with $\mathbf{N}_i = \mathbf{0}$. The middle solid (red) line shows the average of 200 similar calculations, with profiles drawn from the same population. The sample behaves almost ballistically at 1 GHz because the defect length is only $\lambda/50$. The sample also behaves ballistically at 25 GHz, where the defect length is $\lambda/2$. The average transmission is at a minimum at 12.5 GHz, where the defect length is $\lambda/4$. In the parlance of localization, this frequency corresponds to the Ioffe-Regel criterion $k\xi = 1$, where the structure correlation length ξ is some fraction of the phonon wavelength $\lambda = 2\pi/k$. In the context of transmission-line theory, localization is greatest when $k\xi = \pi/2$ because, upon moving along the structure and looking back along the structure, the variation in impedance is greatest when the defect length is $\lambda/4$. At this frequency, the proportionate uncertainty in transmission is large, as evidenced by the top and bottom (green) lines, which show the one-standard-deviation limits.

The effect of localization in bulk glassy materials has been studied extensively in recent years. It is believed to be the cause of a plateau in thermal conductivity and a peak in heat capacity over 1–10 K. This temperature range implies a structure correlation length of 20–50 Å,[46] which is consistent with the microstructure of disordered dielectrics.[47] Care is required, however, because the deposition and processing conditions affect the properties and microstructure of Si_xN_y greatly, and other materials can be very different. In addition, resonant scattering is influential even when the wavelength is 10 times larger than the Ioffe-Regel criterion would suggest, and defects in microbridges are proportionately more significant than defects in bulk. Thus, resonant scattering is likely to play a role in determining the behavior of microbridges. In our own experimental work, the variation in the thermal conductances of notionally identical samples having $t = 0.2$ μm, $b = 1.0$ to 5.0 μm, and $l = 200$ to 600 μm is around $\pm 15\%$, which cannot be accounted for by nonlocalized calculations based on surface-roughness measurements. Although Fig. 7 indicates that *on average* resonant scattering forms a low-pass filter, in reality, the transmission of a single sample varies rapidly with frequency, and it is the rapid frequency variation that leads to a reduction in the frequency-integrated flux. For temperatures below 0.5 K, there is little power in the Planck spectrum above 25 GHz, and the filtering effect of the disorder is great. If the structure correlation length is much smaller than the value used, 0.2 μm, then the effective passband extends to higher frequencies. It is also possible to allow the cell lengths to vary randomly according to some distribution, but we shall not do so here.

Although we have used the word "localization," it has not been shown that the model produces the characteristics of localized transport. Figure 8 shows, as solid (black) lines, flux as a function of length for microbridges having $b = 1.0 \pm 0.1$, 1.0 ± 0.2, 1.0 ± 0.3 and 1.0 ± 0.4. $T_h = 0.3$ K, $T_c = 0$ K, the defect length was set to $\Delta l/\lambda = 0.02$ at 1 GHz, and $\nu = 5$ GHz. In each case, the behavior of 200 randomly chosen samples were averaged to give a mean flux. Each length constitutes a complete new calculation because, when resonant scattering is present, it is not appropriate to infer the behavior of a set of short samples by simulating the behavior of a single long sample. The flux of a single sample does not even decrease monotonically with length. Each curve comprises 20 000 simulations. Figure 8 shows evidence of three kinds of transport: (i) For very short samples, the flux limits to the ballistic value $I = I_0 = 2.7$ fW/GHz. (ii) As the samples are made

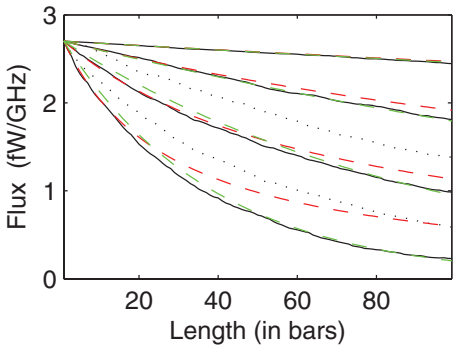

FIG. 8. (Color online) Flux through a series of microbridges having elastic scattering only. $T_h = 0.3$ K, $T_c = 0.1$ K, and $\nu = 5$ GHz. 200 randomly chosen samples were averaged in each case. The solid (black) lines, top to bottom, correspond to Gaussian populations having $b = 1 \pm 0.1$, 1 ± 0.2, 1 ± 0.3, 1 ± 0.4. The dotted lines show the one-standard-deviation limits in the $b = 1 \pm 0.3$ case. The dashed lines show the diffusive (red) and localized (green) models described in the text.

longer, there is a region of elastic diffusive behavior, which decreases in extent as the roughness is increased. The dashed (red) lines correspond to the models $I = I_o[1.0 + L/L_{\rm dif}]^{-1}$, with $L_{\rm dif} = 1050, 240, 71, 28$ cells, respectively. Models that describe the behavior of short samples fail to describe the behavior of long samples. (iii) The dashed (green) lines show the models $I = I_o \exp[-L/L_{\rm loc}]$, with $L_{\rm loc} = 1050, 240, 94, 38$, which corresponds to localized transport. The localization length $L_{\rm loc}$ decreases as the roughness increases. It is not possible to fit the data with diffusive or localized models alone. There is evidence of a diffusive-to-localized transition, where the crossover length depends on frequency and the statistics of the edge profile. In this simulation, the wavelength was five times the defect length, corresponding to 2.5 GHz in Fig. 7. Thus, although the effects seem small in the frequency response, they can lead to localized behavior in long samples. These observations suggest that localization can be significant in Si_xN_y microbridges having lengths of a few microns. The dotted lines in Fig. 8 show the one-standard-deviation limits for the case $b = 1.0 \pm 0.3$. The proportional uncertainty in flux increases markedly with length, showing that the behavior of a long sample is less predictable than the behavior of a short sample. The spread in behavior indicates that it would not be possible to observe the diffusive to localized transition in measurements taken on single samples having different lengths. These are known characteristics of localized transport.[21]

Figure 9 explores the effect of inelastic scattering on localization. The top plot shows the cross section of a microbridge taken from a Gaussian population having $b = 1 \pm 0.2$. $T_h = 0.3$ K, $T_c = 0$ K, the defect length was $\Delta l/\lambda = 0.02$ at 1 GHz, and $\nu = 10$ GHz. The top solid (black) line of the middle plot shows the forward-traveling flux for $G = 0.999\,999$, essentially elastic scattering only. Because the behavior is undamped, there is appreciable resonant scattering near the hot termination. The net flux is 2.9×10^{-3} fW/GHz. Other samples drawn from the same population show a variety of behavior, but there is a tendency for energy to be stored near the exciting termination, leading to an increase in local heat capacity. It is very difficult to attribute trapping to specific features in the profile. The bottom solid (red) line of the middle plot shows the flux with $G = 0.9$, corresponding to the introduction of inelastic scattering. The dotted red line shows the net flux, which is 98.3×10^{-3} fW/GHz. When inelastic scattering is introduced, resonant scattering is damped, and the stochastic filter starts to leak due to inelastic diffusive transport. The forward- and reverse-traveling fluxes, not shown, become near-linear functions of position, as in Fig. 4, but with steps at positions of greatest reflection. The bottom plot in Fig. 9 shows the temperature distributions. In the nearly lossless case, the temperature changes abruptly at about half way along the sample, whereas in the heavily damped case, the temperature changes smoothly with position, reflecting the form of the Planck function.

Consider the behavior of macroscopically patterned components when ballistic, elastic diffusive, localized, and inelastic diffusive scattering are present. Figure 10 shows the profile of an acoustic Fabry-Perot resonator having a normalized width of 4.0 and length of 10 bars. The top plot in each case shows the profile used. It was simulated at the 2λ

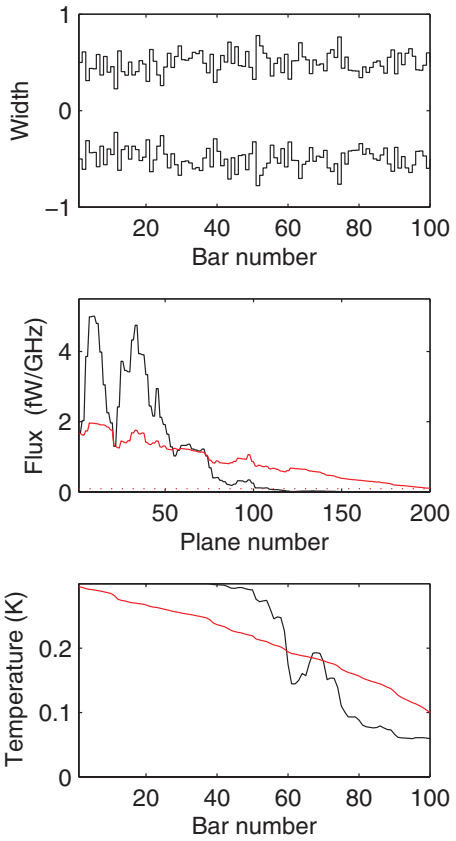

FIG. 9. (Color online) Top: Width as a function of position, taken from a Gaussian distribution having $b = 1 \pm 0.2$. $T_h = 0.3$ K, $T_c = 0$ K, and $\nu = 10$ GHz. Middle: The top solid (black) and bottom (red) lines show the forward-traveling fluxes as a function of position for $G = 0.999\,999$ and $G = 0.9$, respectively. The dotted (red) line shows the net flux for the inelastic case. Bottom: The corresponding temperature distributions.

resonant frequency $\nu = 20$ GHz, with the terminations held at $T_h = 0.3$ K and $T_c = 0$ K. Although we have modeled more complicated components, including multi-element filters and tapers having a variety of edge profiles and random distributions of cell losses, lengths, and widths, here we discuss a simple structure in order that the main features of the method can be appreciated. Initially, $G = 0.99$. The left-middle plot shows the fluxes traveling to the right [upper (green) line] and left [lower (red) line] as a function of position. The dashed (black) line is the net flux, which must be the same everywhere at equilibrium. At the cold end there is no backward flux because the termination is matched. There is a circulating flux in the resonator, corresponding to the Debye heat capacity of the central section. The presence of inelastic scattering and associated reradiation by losses causes a linear gradient in the fluxes, and a backward-traveling flux at the hot termination. Because the attenuation length is greater than the length of the central section, the structure retains the characteristics of a resonator. The bottom plot shows the temperature distribution of the losses. In the right column, $G = 0.5$. The attenuation length is now much smaller than the length of the resonator, and resonant behavior is lost. The losses accrue a temperature gradient, and the diffusive process that results is essentially the same as if the resonator were not present. Diffusion causes a

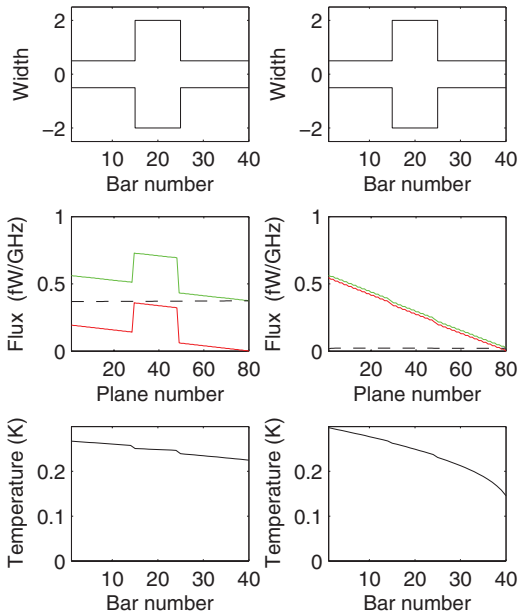

FIG. 10. (Color online) Left column, top: Width profile of a Fabry-Perot resonator. $T_h = 0.3$ K, $T_c = 0$ K, $\nu = 20$ GHz, and $G = 0.99$. Middle: The top (green) and bottom (red) lines show the flux traveling to the right and left, respectively. The dashed (black) line is the net flux. Bottom: The temperature distribution of the losses. Right column: The same as the left column, but with $G = 0.5$.

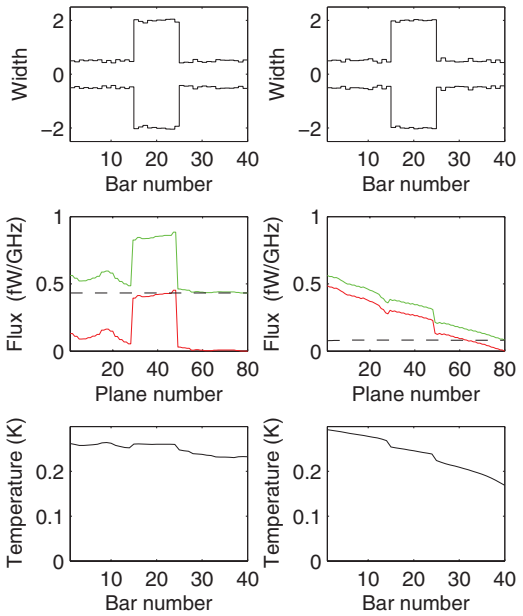

FIG. 11. (Color online) Left column, top: Width profile of a Fabry-Perot resonator having an edge roughness of ± 0.1. $T_h = 0.3$ K, $T_c = 0$ K, $\nu = 20$ GHz, and $G = 0.999\,999$. Middle: The top (green) and bottom (red) lines show the flux traveling to the right and left, respectively. The dashed (black) line is the net flux. Bottom: The temperature distribution of the losses. Right column: The same as the left column, but with $G = 0.9$.

lowering of transmission in band, and a leakage of power out of band.

Figure 11 shows the behavior of the same resonator, again at $\nu = 20$ GHz, but with elastic scattering only, $G = 0.999\,999$, brought about by a random edge profile: ± 0.1. There is phonon trapping approximately 10 cells to the left of the leading edge of the resonator, which corresponds to a few wavelengths. We often see an enhancement of resonant trapping between the edges of patterned features and random variations in microstructure. This observation shows that the local heat capacity is also enhanced. The right column of Fig. 11 shows the effect of introducing inelastic scattering, $G = 0.9$. The loss suppresses localization, and diffusive transport becomes dominant, causing the component to behave as an ordinary thermal conductor.

Figure 12 shows the frequency response of the Fabry-Perot resonator shown in Fig. 10. The top solid (red) line shows the transmitted power when $G = 0.999\,999$, corresponding to resonant ballistic transport. The middle solid (green) line shows the case when $G = 0.999$, but with no diffusive transport; whereas the dashed (green line) shows the transmitted power when diffusion is allowed. The curves are similar, because the attenuation over the length of the resonator is small, maintaining the same loaded Q, but the diffusive case shows a higher flux due to diffusive transport along the legs outside of the resonator. The bottom solid (blue) line shows the response when $G = 0.99$, with no diffusion, whereas the bottom dashed (blue) line shows the response when diffusion is allowed. Again, the total flux is higher due to diffusion. It is clear that when considering the behavior of lossy phononic filters, it is necessary to distinguish between the characteristics being degraded by the reduction of Q, and the degradation caused by inelastic diffusion,

Now turn to multimode simulations. Figure 13 shows the forward-traveling fluxes in the longitudinal (black), torsional (blue), out-of-plane flexure (green), and in-plane-flexure (red) modes as a function of position for a 0.2-μm-thick sample of Si_xN_y. We ignore higher-order modes for simplicity. The forward-traveling fluxes at plane 200 also correspond to the next fluxes in the individual modes. Elastic scattering was

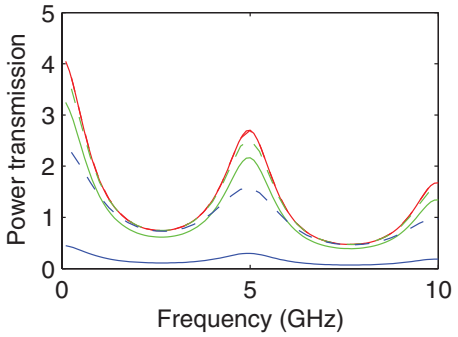

FIG. 12. (Color online) Frequency response of the Fabry-Perot resonator shown in Fig. 10. $T_h = 0.3$ K, $T_c = 0$ K. The top solid (red) line shows the transmitted power when $G = 0.999\,999$, corresponding to ballistic resonant transport. The middle solid (green) line shows the case when $G = 0.999$, but with no diffusive transport. The dashed (green line) shows the transmitted power when diffusion is introduced. The bottom solid (blue) line shows the case with $G = 0.99$, but without diffusion, and the bottom dashed (blue) line is with diffusion.

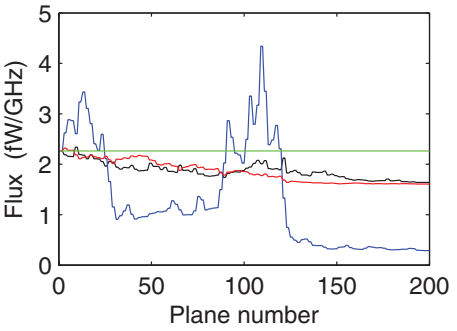

FIG. 13. (Color online) Forward flux as a function of position for a multimode Si_xN_y microbridge having elastic scattering only. The width was taken from a Gaussian population having $b = 1.0 \pm 0.1$. $T_h = 0.2$ K, $T_c = 0$ K, $\nu = 1.6$ GHz, and the length of each cell was 0.39 μm, giving a total length of 39 μm. The individual curves correspond to the longitudinal (black), torsional (blue), in-plane flexure (red), and out-of-plane flexure (green) modes.

included in the form of a randomly varying width drawn from a Gaussian population having $b = 1.0 \pm 0.1$. $T_h = 0.2$ K, $T_c = 0$ K, and $\nu = 1.6$ GHz. The cell length was 0.39 μm, giving a total length of 39 μm. Although intermodal scattering was not included, the results were calculated simultaneously using the multimode model, and intermodal scattering could have been easily included. By inspecting Figs. 2 and 3, the results of the multimode simulation shown in Fig. 13 can be understood as follows: (i) The torsional mode (blue) is sensitive to step changes in width and has a wavelength of 4.0 cells at 1.6 GHz. Each cell is therefore $\lambda/4$ long, and the mode is localized, with a severely attenuated flux. (ii) The out-of-plane flexural mode (green) has a wavelength of 4 cells but is insensitive to changes in width and therefore behaves ballistically. (iii) The longitudinal mode (black) has a wavelength of 16.5 cells and has a moderate sensitivity to step changes in width. It shows some trapping, but the position dependence of the flux suggests an elastic-diffusive form. (iv) The in-plane flexural mode has a wavelength of 9.0 cells and a moderate sensitivity to width. It, too, shows a diffusive form. Although not explicit in this plot, we have found that localization does not occur in the flexural modes when the structure correlation length is $\lambda/4$ because the imaginary parts of the reflection coefficients modify the condition at which resonance takes place. The ballistic nature of the out-of-plane flexural mode is a recurrent theme in many simulations. It seems that a phononic filter should have patterned changes in both thickness and width if the in-plane and out-of-plane flexural modes are to be attenuated. Interestingly, step changes in width and thickness can be made at different planes, in order to take into account the different modal wavelengths. Experimental work on membranes has shown that heat flux is sensitive to micromachined surface features.[48] Although not studied here, we would expect intermodal scattering to reduce localization in a way that is consistent with the generic characteristics of localization in two and three dimensions.

Figure 14 shows the situation where a resonant section is placed in the multimode transmission structure of Fig. 13. The central resonator was 31 bars long, corresponding to 31.39 μm, and $b = 4.0$ wide. We do not include a higher

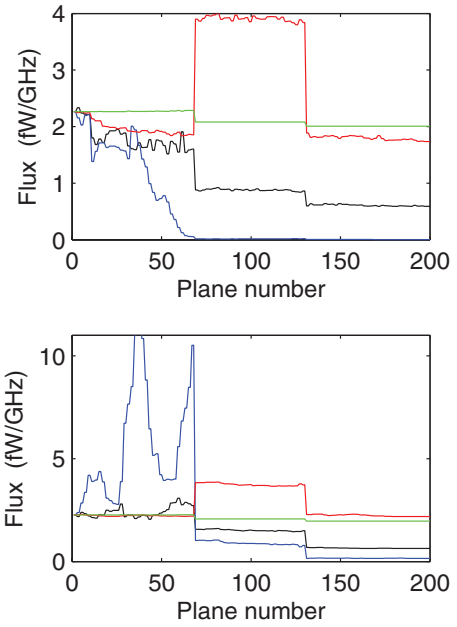

FIG. 14. (Color online) Top and bottom: Two statistical realizations, drawn from a Gaussian population having an edge roughness of ± 0.1, of a multimode Fabry-Perot interferometer. The same parameters were used as for Fig. 13, $T_h = 0.2$ K, $T_c = 0$ K, $\nu = 1.6$ GHz, but with a central resonator 31 bars long, corresponding to 31.39 μm, and $b = 4.0$ wide. The individual curves correspond to the longitudinal (black), torsional (blue), in-plane flexure (red), and out-of-plane flexure (green) modes.

number of propagating modes in the central section, or evanescent modes, which would contribute to the heat capacity. The individual curves correspond to the longitudinal (black), torsional (blue), in-plane flexure (red), and out-of-plane flexure (green) modes. The top plot has a number of features. The cavity is resonant in the in-plane flexural mode (red), leading to high transmission. The out-of-plane flexural mode also shows high transmission, because large steps in width only result in small reflection coefficients. The longitudinal mode (black) is off resonancebecause of its different wavelength and shows a lower overall transmission factor. The modes show varying degrees of localization, which depend on the degree to which edge roughness introduces scattering. The torsional mode (blue) is scattered so strongly that the flux is very low once the wave reaches the resonator, showing almost no stored energy in the resonator itself. The bottom plot shows a calculation having the same parameters, but using a different sample from the same statistical population. The flexural and longitudinal modes behave in much the same way as before (note the change in scale), with a tendency for energy to be stored to the left of the leading edge, which is due to resonant interaction between the edge of the resonator and localized cells. The strongly scattered torsional mode shows a high level of localization to the left of the leading edge, and low overall transmission. It seems that the existence of sharp edges can lead to a higher heat capacity than would be calculated purely on the basis of the resonator alone.

Although the behavior is complicated, the prospects for using patterned structures to minimize heat flow are good. Those modes that are strongly elastically scattered, giving

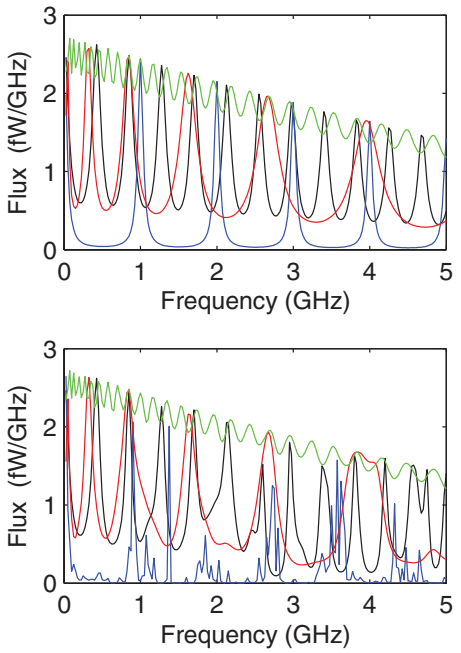

FIG. 15. (Color online) Frequency response of Fabry-Perot filter of Fig. 14. The top plot shows the modal powers for a structure with perfectly smooth edges, whereas the bottom plot shows the modal powers for the same structure, but with an edge roughness chosen from a Gaussian population having ± 0.1. $T_h = 0.2$ K, $T_c = 0$ K. The individual curves correspond to the longitudinal (black), torsional (blue), in-plane flexure (red), and out-of-plane flexure (green) modes.

localized transport, tend to result in small fluxes, or they are scattered strongly at edges, resulting in a reduction in flow either by Fabry-Perot resonances or by scattering at discontinuities. Those modes that are weakly scattered can be filtered by resonators. Diffusive transport can cause filters to leak, but if the leads, as distinct from the resonator, are made long enough, diffusive transport can be put to good benefit.

Figure 15 shows the frequency response of the Fabry-Perot filter of Fig. 14. The top plot shows the modal powers for a structure with perfectly smooth edges, whereas the bottom plot shows the modal powers for the same structure, but with an edge roughness chosen from a Gaussian population having a width of ± 0.1. $T_h = 0.2$ K, $T_c = 0$ K. The individual curves correspond to the longitudinal (black), torsional (blue), in-plane flexure (red), and out-of-plane flexure (green) modes. The total flux, not shown, is the sum of the four curves. In the top plot notice that the Fabry-Perot effect is most pronounced for the torsional mode, and least pronounced for the out-of-plane flexural mode. The positions of the resonances reflect the dispersion relationships of Fig. 2. Even for this simple structure, where the individual modes behave differently, there is an overall filtering compared with the blackbody spectrum at $T_h = 0.2$ K, which is traced by the upper envelope of the curves. The bottom plot of Fig. 15 shows the behavior of the same resonator, but with a variation in width of ± 0.1 along the whole length of the structure. The out-of-plane flexural mode (green) is affected little by the roughness, whereas the in-plane flexure (red) and longitudinal (black) modes show that certain of the peaks are shifted due to resonant trapping. Nevertheless, on average a significant amount of filtering takes place. The torsional mode (blue) is heavily attenuated by localization, and the interaction between the localized cells and the edges of the resonator.

A number of generic factors should be borne in mind when designing thermal filters. The filtering may not be due to a single order of a resonator, but averaged over many periods. Even when the acoustic modes have different dispersion relationships, the overall flux can still be reduced significantly, particularly if resonators are defined in terms of width and thickness to take into account the different dispersion relationships of the in-plane and out-of-plane flexural modes. Localization may limit the contributions of certain modes, but patterning can still be used to resonantly filter the highly transmissive modes. The heat capacity may be seen to increase unexpectedly due to interactions between patterned edges and defects. Filtering may take place through nonresonant or resonant scattering, depending on whether the scale size of the patterned features is greater or smaller than the acoustic attenuation length. An interesting idea is to use short resonators separated by large distances to achieve phase isolation through diffusive conduction.

V. CONCLUSIONS

A model has been described for simulating the low-temperature thermal behavior of low-dimension components patterned into amorphous dielectric membranes. The model uses directed flow graphs together with a nonlinear root-finding algorithm to accommodate ballistic, elastic diffusive, localized, and inelastic diffusive scattering. Different statistical models can be used to represent the microstructure. A parametric dependency of acoustic loss on frequency[30] can be incorporated. The technique not only gives the average behavior of structures, but also the spread in behavior of notionally identical devices. Our intention is to use the method to devise experiments that allow material parameters to be determined and to attempt to design microscopic structures that minimize heat flow and thermal noise. Many extensions are possible: For example, the technique could be used to model multiport components, such as several microbridges supporting a central island, or cast into other basis sets to allow cross-plane heat calculations in superlattices.[49] The next phase of the work is to use elasticity theory to calculate the dispersion relationships of microbridges having different cross sections, to include evanescent waves, and to create a library of scattering parameters for discontinuities of various kinds.

*stafford@mrao.cam.ac.uk

[1]F. Giazotto, T. T. Heikkilä, A. Luukanen, A. M. Savin, and J. P. Pekola, Rev. Mod. Phys. **78**, 217 (2006).

[2]Y. Dubi and M. Di Ventra, Rev. Mod. Phys. **83**, 131 (2011).

[3]M. P. Blencowe, Phys. Rev. B **59**, 4992 (1999).

[4]D. V. Anghel, J. P. Pekola, M. M. Leivo, J. K. Suoknuuti, and M. Manninen, Phys. Rev. Lett. **81**, 2958 (1998).

[5]D. J. Goldie, A. V. Velichko, D. M. Glowacka, and S. Withington, J. Low Temp. Phys. **167**, 248 (2012).
[6]D. J. Goldie, D. M. Glowacka, K. Rostem, and S. Withington, in *Proceedings of the 21st International Symposium on Space Terahertz Technology* (University of Oxford, Oxford, 2010), p. 85, http://www.nrao.edu/meetings/isstt/.
[7]D. J. Goldie, A. V. Velichko, D. M. Glowacka, and S. Withington, J. Appl. Phys. **109**, 084507 (2011).
[8]K. Rostem, D. M. Glowacka, D. J. Goldie, and S. Withington, *in Millimeter and Submillimeter Detectors and Instrumentation for Astronomy*, Proc. SPIE, 7020 (SPIE, Bellingham, 2008).
[9]K. Rostem, D. J. Goldie, S. Withington, D. M. Glowacka, V. N. Tsaneva, and M. D. Audley, J. Appl. Phys. **105**, 084509 (2009).
[10]K. Schwab, E. A. Henriksen, J. M. Worlock, and M. L. Roukes, Nature (London) **404**, 974 (2000).
[11]L. G. C. Rego and G. Kirczenow, Phys. Rev. Lett. **81**, 232 (1998).
[12]K. R. Patton and M. R. Geller, Phys. Rev. B **64**, 155320 (2001).
[13]B. A. Glavin, Phys. Rev. Lett. **86**, 4318 (2001).
[14]R. Lifshitz, and M. L. Roukes, Phys. Rev. B **61**, 5600 (2000).
[15]O. B. Wright and W. A. Phillips, Philos. Mag. B **50**, 63 (1984).
[16]P. W. Anderson, B. I. Halperin, and C. M. Varma, Philos. Mag. **25**, 1 (1971).
[17]R. C. Zeller and R. O. Pohl, Phys. Rev. B **4**, 2029 (1971).
[18]C. C. Yu and J. J. Freeman, Phys. Rev. B **36**, 7620 (1987).
[19]B. L. Zink and F. Hellman, Solid State Commun. **129**, 199 (2004).
[20]B. L. Zink, R. Pietri, and F. Hellman, Phys. Rev. Lett. **96**, 055902 (2006).
[21]A. Kundu, A. Chaudhuri, D. Roy, A. Dhar, J. L. Lebowitz, and H. Spohn, Europhys. Lett. **90**, 40001 (2010).
[22]I. Savić, N. Mingo, and D. A. Stewart, Phys. Rev. Lett. **101**, 165502 (2008).
[23]T. Yamamoto, K. Sasaoka, and S. Watanabe, Phys. Rev. Lett. **106**, 215503 (2011).
[24]D. H. Santamore and M. C. Cross, Phys. Rev. B **66**, 144302 (2002).
[25]D. H. Santamore and M. C. Cross, Phys. B (Amsterdam, Neth.) **316-317**, 389 (2002).
[26]D. V. Anghel, T. Kühn, Y. M. Galperin, and M. Manninen, Phys. Rev. B **75**, 064202 (2007).
[27]G. Chen, Phys. Rev. Lett. **86**, 2297 (2001).
[28]M. Von Haumeder, U. Strom, and S. Hunklinger, Phys. Rev. Lett. **44**, 84 (1980).
[29]R. O. Pohl, X. Liu, and E. Thompson, Rev. Mod. Phys. **74**, 991 (2002).
[30]S. Withington, D. J. Goldie, and A. V. Velichko, Phys. Rev. B **83**, 195418 (2011).
[31]A. D. Olver, P. J. B. Clarricoats, A. A. Kishk, and L. Shafai, *Microwave Horns and Feeds* (IEE Electromagnetic Waves Series 99, The Institution of Electrical Engineers, London, 1994), Chap. 4.
[32]N. Nishiguchi, Y. Ando, and M. N. Wybourne, J. Phys.: Condens. Matter **9**, 5751 (1997).
[33]A. Gusso and L. G. C. Rego, Phys. Rev. B **75**, 045320 (2007).
[34]H. Bosma, Philips Res. Rep., Suppl. **10**, 1 (1967).
[35]S. W. Wedge and D. B. Rutledge, IEEE Microwave and Guided Wave Lett. **1**, 117 (1991).
[36]K.-Q. Chen, W.-X. Li, W. Duan, Z. Shuai, and B.-L. Gu, Phys. Rev. B **72**, 045422 (2005).
[37]L.-M. Tang, L.-L. Wang, K.-Q. Chen, W.-Q. Huang, and B. S. Zou, Appl. Phys. Lett. **88**, 163505 (2006).
[38]X.-F. Peng, K.-Q. Chen, and B. S. Zou, Appl. Phys. Lett. **90**, 193502 (2007).
[39]M. C. Cross and R. Lifshitz, Phys. Rev. B **64**, 085324 (2001).
[40]S. V. J. Narumanchi, J. Y. Murthy, and C. H. Amon, J. Heat Transfer **125**, 896 (2003).
[41]A. A. Joshi and A. Majumdar, J. Appl. Phys. **74**, 31 (1993).
[42]T. Klitsner, J. E. VanCleve, H. E. Fischer, and R. O. Pohl, Phys. Rev. B **38**, 7576 (1988).
[43]J. Jäckle, Solid State Commun. **39**, 1261 (1981).
[44]A. Kambili, G. Fagas, V. I. Fal'ko, and C. J. Lambert, Phys. Rev. B **60**, 15593 (1999).
[45]N. Perrin, Phys. Rev. B **48**, 12151 (1993).
[46]J. E. Graebner, B. Golding, and L. C. Allen, Phys. Rev. B **34**, 5696 (1986).
[47]S. K. Watson and R. O. Pohl, Phys. Rev. B **68**, 104203 (2003).
[48]V. Yefremenko *et al.*, Appl. Phys. Lett. **94**, 183504 (2009).
[49]G. Chen, Phys. Rev. B **57**, 14958 (1998).